Static Attitude Stability of Deep Space Sample Return Capsule with Thin Aeroshell

Hideto Takasawa,[a*] Tomoya Fujii,[b] Yusuke Takahashi,[c] Takahiro Moriyoshi,[d] Hiroki Takayanagi[e], Yasunori Nagata,[d] and Kazuhiko Yamada[d]

[a]*Division of Mechanical and Space Engineering, Hokkaido University, Kita 13 Nishi 8, Kita-ku, Sapporo, 060-8628, Hokkaido, Japan,*

**corresponding author, thide3224@eis.hokudai.ac.jp, ORCID:0000-0002-9476-5703*

[b]*Department of Applied Mechanics and Aerospace Engineering, Waseda University, 3-4-1 Okubo, Shinjuku, 169-8555, Tokyo, Japan*

[c]*Division of Mechanical and Space Engineering, Hokkaido University, Kita 13 Nishi 8, Kita-ku, Sapporo, 060-8628, Hokkaido, Japan*

[d]*Institute of Space and Astronautical Science, Japan Aerospace Exploration Agency, 3-1-1 Yoshinodai Chuo-ku, Sagamihara, 252-5210, Kanagawa, Japan*

[e]*Research and Development Directorate, Japan Aerospace Exploration Agency, 3-1-1 Yoshinodai Chuo-ku, Sagamihara, 252-5210, Kanagawa, Japan*

A sample return mission to deep space has been proposed. The orbital velocity of the deep space sample return capsule (DS-SRC) during atmospheric entry reaches 15 km/s, which results in extremely severe aerodynamic heating to the sample return capsule. We proposed a new concept of the DS-SRC with a lightweight and large-area aeroshell to reduce the severe heating environment at high altitudes through efficient aero-deceleration. The DS-SRC must be aerodynamically stable at all speeds because it is expected to be operated without a parachute at atmospheric entry. First, we showed the flight environment of the DS-SRC along the atmospheric entry trajectory obtained by trajectory analysis. Second, we investigated the aerodynamic characteristics and the static stability in the all-speed range using low-speed, transonic, and supersonic wind tunnels. Last, we used a computational science approach to conduct unsteady turbulent flow simulations to show its stability mechanism. The trajectory analysis indicated that the peak heat flux at the stagnation point of the capsule was kept approximately 10 MW/m^2 when decelerating from high altitude because of its low ballistic coefficient. Based on the wind tunnel experimental results, we confirmed that this capsule is statically stable in attitude at all speeds. Furthermore, the computed results suggested that there is a difference in pressures at the windward and leeward sides of the front surface when the capsule is pitched up or down. This difference in pressure distribution acts as a static stability mechanism generating a moment in the direction that restores the pitching motion.

Key Words: Static stability · computational fluid dynamics · particle image velocimetry ·

reentry capsule

Statements and Declarations

The authors have no competing interests to declare that are relevant to the content of this article.

List of Symbols

C	aerodynamic coefficient
C_s	Smagorinsky constant
C_w	empirical constant of Smagorinsky model
D	distance from wall, m
g	gravity acceleration, m/s^2
S_{ij}	strain-rate tensor, s^{-1}
Δ	grid scale
k	von Karman constant
μ	viscosity, N s/m^2
ρ	density, kg/m^3

Subscripts

D	drag
L	lift
M	pitching moment
P	pressure
SGS	sub grid scale

1. Introduction

A sample return mission for deep space exploration has been proposed, designed to travel to farther planets or asteroids from the Hayabusa missions. In the atmospheric reentry phase, there are severe problems, such as aerodynamic heating because a capsule's orbital velocity reaches 15 km/s, assuming a sample return from Saturn, which is a higher velocity than the Hayabusa mission of 12 km/s.

Therefore, we proposed the novel concept of a capsule [1] to overcome this challenge and achieve deep space exploration. Figure 1 shows an image of a thin aeroshell capsule. This capsule is lightweight and has a large surface area for efficient aero-deceleration at high altitudes to avoid heating. Additionally, this rigid capsule with a thin aeroshell can overcome more severe aerodynamic heating caused by the high reentry velocity when compared to an inflatable aerodynamic decelerator [2,3] with the same concept.

One option for achieving a lower ballistic coefficient is to increase the aeroshell size. However, this would result in an increase in the mass of the aeroshell and a shift in the center of gravity downstream. Consequently, this negatively influences aerodynamic stability. Therefore, it is important to evaluate the stability of a capsule designed with a large aeroshell to account for aerodynamic deceleration.

Understanding aerodynamic characteristics, such as the attitude instability of the thin aeroshell capsule, is essential to improving the safety and probability of succeeding in an atmospheric entry mission. In the worst case, aerodynamic instability in attitude can cause problems such as insufficient aero-deceleration. Additionally, if the vehicle's attitude motion diverges, there is a possibility of landing at a point that deviates from the predicted landing site. Such aerodynamic instability was observed for the inflatable reentry vehicle by the JAXA S-310-41 sounding rocket (SMAAC), which has a similar shape to the present capsule at low speeds (M = 0.1) [4], and for the Hayabusa capsule [5] in the transonic region (M = 1.1).

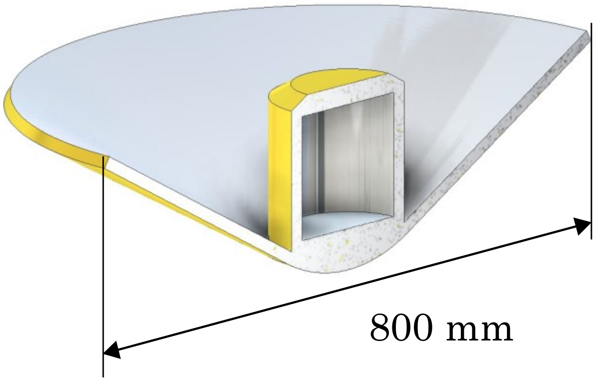

(a) Thin-shell type capsule

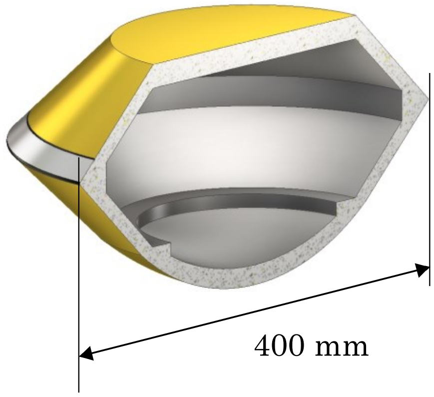

(b) Hayabusa capsule

Fig. 1 Images of capsules

An approach to mitigate aerodynamic instability is in high demand because the present capsule is designed to descend without a parachute. This means that stability in attitude at all speeds, including low speeds, must be secured.

Aerodynamic instability refers to an oscillation or rotation of the reentry vehicle caused by aerodynamic force during flight, and it has been discussed from two perspectives: static stability and dynamic stability [6]. The static stability was evaluated based on moment curves according to the angle of attack (AOA) in a stationary state. If there is a negative moment from a positive AOA and a positive moment from a negative AOA, this moment returns the AOA to zero degrees or cancels the change in AOA, which means it is statically stable. Second, dynamic stability is evaluated when there is an angular velocity around the center of gravity. A vehicle in a dynamic stable state always dampens the angular velocity. The AOA converges to zero if the vehicle is statically stable. Therefore, ensuring both static and dynamic stability is necessary because the oscillatory motion of a vehicle diverges when one of the stabilities is lost.

There are several factors [7] that affect these instabilities, such as the position of the center of gravity [8], the angle of the front surface [9], and the length and roundness of the rear [10,11]. For dynamic instability, pressure phase delay [12] and reattachment [13] have been considered as the factors. However, a complete method for mitigating aerodynamic instability at all speeds has not yet been proposed. Moreover, the aerodynamic characteristics of the capsule have been insufficiently obtained.

The objectives of this study were to evaluate the static stability of a thin aeroshell capsule and to reveal its stability mechanism. This paper is the first of the series on DS-SRC attitude instability studies and focuses on the static. Dynamic stability study, which is partly discussed in our work [14], is the future step.

Here, firstly we carried out a reentry trajectory analysis to obtain the flight conditions and determine the experimental conditions. Then, we reproduced the reentry environment using a 2 m × 2 m low-speed wind tunnel (LWT), Institute of Space and Astronautical Science (ISAS) transonic wind tunnel (TWT), and ISAS supersonic wind tunnel (SWT) at the Japan Aerospace Exploration Agency (JAXA). We fixed the capsule at an AOA and obtained its aerodynamic coefficients during the experiments. In addition, we conducted particle image velocimetry (PIV) to obtain the wake in the LWT. Furthermore, we conducted turbulent flow simulations using a computational fluid dynamics (CFD) approach to investigate the static stability mechanism for each condition.

2. Reentry trajectory

2.1. Flight environment in reentry trajectory

We conducted a trajectory analysis to obtain the flight environment of the thin aeroshell capsule during reentry. The analysis conditions from previous studies [1,15] are shown in Table 1. Furthermore, those over a wide range were set in this analysis because the drag coefficient of the thin aeroshell capsule was unclear. Additionally, a comparison was made with the Hayabusa capsule, which has successfully achieved sample return. The Hayabusa capsule used a parachute during the actual flight. However, the present trajectory analysis of this capsule was performed assuming no parachute to compare the terminal velocities at landing. The analysis models were implemented on the Tacode [16], developed by Takahashi et al. We assume that the capsule is a point mass on an Earth-centered, Earth-fixed (ECEF) non-inertial frame. Additionally, the earth's gravitational force as well as the Coriolis, centrifugal, and aerodynamic forces act on this point mass. In this case, the equation of motion is given by

$$m\frac{\partial^2 \boldsymbol{x}}{\partial t^2} = \boldsymbol{F}_{\mathrm{grav}} - 2m \cdot \boldsymbol{\omega} \times \boldsymbol{v} - m \cdot \boldsymbol{\omega} \times (\boldsymbol{\omega} \times \boldsymbol{x}) + \boldsymbol{F}_{\mathrm{aero}} \quad (1)$$

Table 1 Trajectory analysis conditions for flight

Capsule	Thin aeroshell capsule	Hayabusa
Software	Tacode v1.12	
Atmosphere Model	NRLMSISE-00 Atmosphere Model [17]	
Initial velocity, km/s	15	11.8
Initial altitude, km	200	200
Initial latitude and longitude, deg	0, 0	0, 0
Flight-path angle, deg	-11	-12.7
Diameter, m	0.8	0.4
Mass, kg	10.0	16.3
Front nose radius, m	0.2	0.2
Drag coefficient	0.8, 1.0, 1.5	1.147

Figure 2 shows the time histories of the altitude, Mach number, and dynamic pressure of the thin aeroshell capsule for $C_D = 1.5$ and the Hayabusa capsule. In the case of a thin aeroshell capsule, the maximum Mach number was approximately 55 at 40 s after reentry, and the maximum dynamic pressure was 8.4 kPa at 70 s. When comparing the Hayabusa capsule with a thin aeroshell capsule, although the initial velocity is high, the ballistic coefficient is small. Therefore, it is possible to reduce the dynamic pressure to less than 1/5 of the Hayabusa case. Due to the same reason, the maximum impact acceleration of the thin aeroshell capsule is 43g, which is smaller than the result of 48g for the Hayabusa capsule.

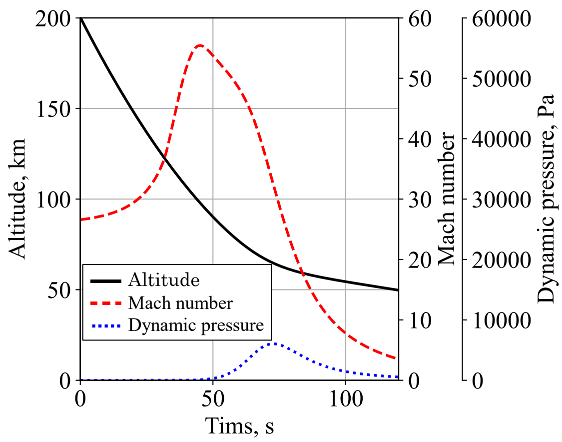

(a) Thin aeroshell capsule for the case $C_D = 1.5$

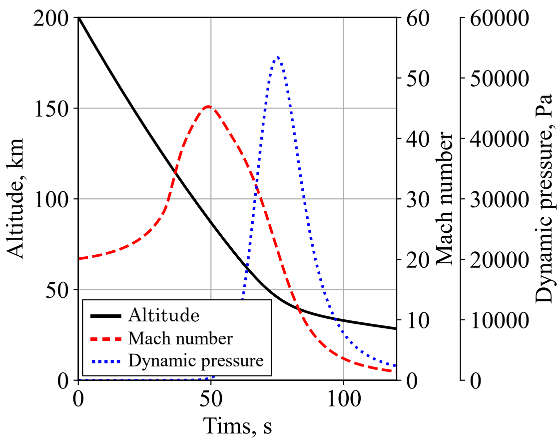

(b) Hayabusa capsule

Fig. 2 Time history of altitude, Mach number and dynamic pressure

The Detra–Kemp–Riddell model [18] was used for convective heating, and the Tauber–Sutton model [19] was used for radiation heating to evaluate the heat flux at the stagnation point, as shown in Equations (2) and (3), respectively, where h represents enthalpy, and we assume that the capsule wall is at a temperature of 300 K. Additionally, R_n refers to the radius of curvature of the front surface, and we have adopted a front nose radius of 0.2 m. As the front nose radius of both capsules is the same, no differences exist in heat flux caused by the curvature radius. The function $f(U_\infty)$ was calculated using linear interpolation.

$$\dot{q}_{con} = \frac{110.35\times10^6}{\sqrt{R_n}}\left(\frac{\rho_\infty}{\rho_{SL}}\right)^{0.5}\left(\frac{U_\infty}{U_{CO}}\right)^{3.15}\left(\frac{h_{stag}-h_w}{h_{stag}-h_{w0}}\right), \frac{W}{m^2} \quad (2)$$

$$\rho_{SL} = 1.225, \mathrm{kg/m^3}$$

$$U_{CO} = 7924.8, \mathrm{m/s}$$

$$\dot{q}_{rad} = 4.736\times10^8 R_n^a \rho^{1.22} f(U_\infty), \frac{\mathrm{W}}{\mathrm{m^2}} \quad (3)$$

$$a = 1.072\times10^6 U_\infty^{-1.88}\rho_\infty^{-0.325}$$

The heat flux profile of the thin aeroshell capsule for the case C_D = 1.5, shown in Fig. 3 indicates that the peak heat flux at the stagnation point was 8.3 MW/m^2. In both cases, Convective heating was dominant. The maximum heat flux of the Hayabusa capsule was 14.6 MW/m^2. The thin aeroshell capsule had a lower peak heat flux owing to its lower ballistic coefficient, resulting in efficient aero-deceleration from high altitudes, despite the higher reentry velocity.

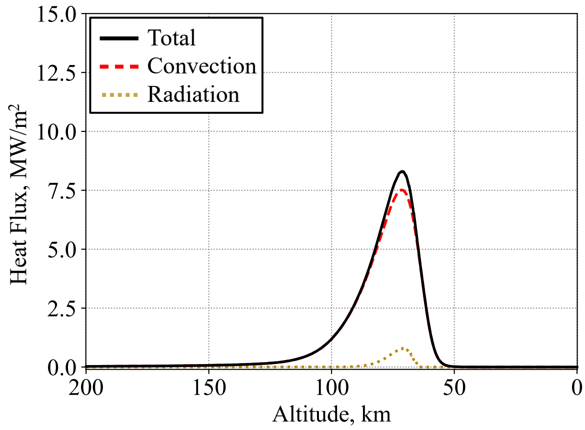

(a) Thin aeroshell capsule for the case C_D = 1.5

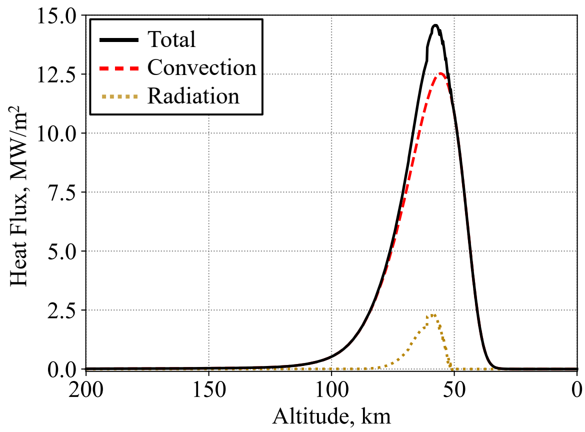

(b) Hayabusa capsule

Fig. 3 Profile of altitude versus heat flux

Figure 4 shows the profile of altitude versus velocity. The thin aeroshell capsule had a lower ballistic coefficient than the Hayabusa capsule. Consequently, the present capsule decelerated at a higher altitude. Table 2 lists the terminal velocity at the landing of each capsule without a parachute. The terminal velocity of the thin aeroshell capsule for C_D = 1.0 was 0.4 times that of the Hayabusa capsule. Elucidation of aerodynamic characteristics is crucial for the accurate prediction of the landing point and estimation of the impact at landing.

Table 2 Comparison of terminal velocity at landing

Capsule	Velocity, m/s
Thin-shell type (C_D=0.8)	19.4
Thin-shell type (C_D=1.0)	17.4
Thin-shell type (C_D=1.5)	14.2
Hayabusa	42.5

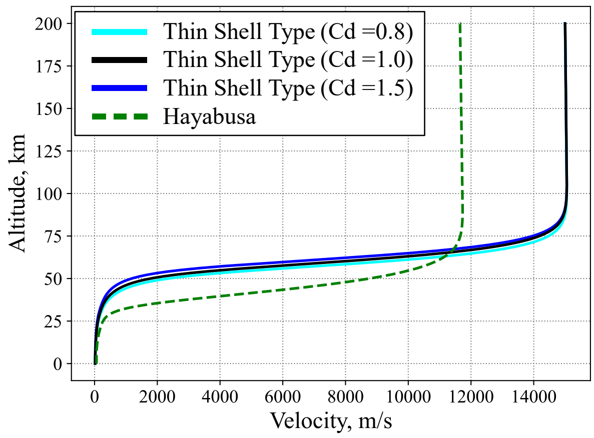

Fig. 4 Profile of altitude versus velocity

3. Wind tunnel tests

The wind tunnel tests were conducted using a JAXA 2 × 2 m low-speed wind tunnel (LWT), ISAS transonic wind tunnel (TWT), and an ISAS supersonic wind tunnel (SWT) to obtain the aerodynamic characteristics of the thin aeroshell capsule at all speeds. Figure 5 shows the flow field conditions for each wind tunnel and atmospheric reentry. The blue circles indicate the values obtained by trajectory analysis. The model diameters for LWT were set to 0.4 m and 0.08 m for TWT and SWT, respectively. To reproduce the flow field during reentry, the Reynolds and Mach numbers should be matched between the flight and wind tunnel experiments. In the LWT, the Reynolds number was close to that during flight, and the Mach number was less than 0.3, where the compressible effect was low. Furthermore, the flight conditions at low speeds could be reproduced in the LWT. Additionally, there was a difference in the Reynolds number between the flight and experiments under the same Mach number in the TWT and SWT. However, in this range, the separation point of the flow near the capsule was clear, and the dependence of the drag coefficient on the Mach number was large. Thus, we focused on the effect of the Mach number.

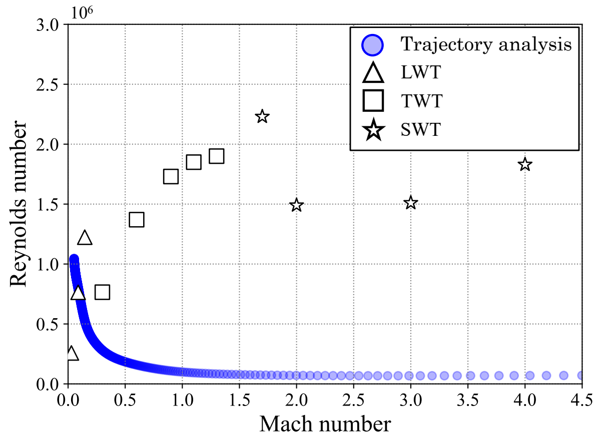

Fig. 5 Test conditions for each wind tunnel and the flow field conditions during reentry

3.1 Low-speed wind tunnel test

The LWT is a continuous, atmospheric closed-circuit type wind tunnel. The test section had a 2 × 2 m square cross-section and was 4 m long. The measurement equipment used is presented in Table 3. A block diagram of the wind tunnel test is shown in Fig.6.

Table 3 Measurement equipment used in the LWT test

Six-components balance	LMC-6528-38/Z200
Pressure gauge for atmospheric pressure	DPI145, GE Druck
Pressure gauge for dynamic pressure	698A, MKS Baratron
Data logger	V743 System

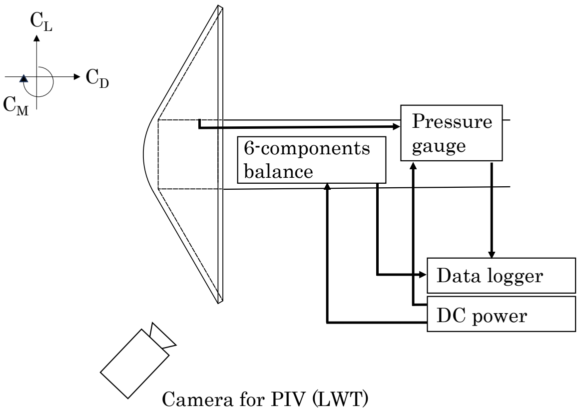

Fig. 6 Block diagram in the low-speed wind tunnel for the thin aeroshell capsule

Figure 7 shows the photo and shape of the capsule used in the experiment. The aerodynamic characteristics were measured using a six-component balance attached to the sting, where the capsule was fixed. The time-averaged aerodynamic coefficients were obtained by measuring for 5 s at a sampling rate of 500 Hz. Furthermore, PIV measurements were taken to determine the wake structure; 2000 images were captured at a sampling rate of 4 Hz with a spatial resolution of 5 mm and a photographing range of 425 × 340 mm. A high-speed camera with a resolution of 3360 pixels × 2712 pixels was used. A 200 mJ Nd:YAG laser was expanded using a cylindrical lens with an f-value of -25 mm, resulting in a measurement range of 425 × 340 mm, which provides a sufficient signal-to-noise ratio (SNR). A spatial resolution of 5 mm was obtained by averaging the processing during PIV analysis to ensure a satisfactory SNR. The PIV setup information for the wind tunnel, excluding the camera and laser, is described in a previous study [20]. Multiple images were superimposed to construct the wake flow field. The mean velocity distributions were obtained.

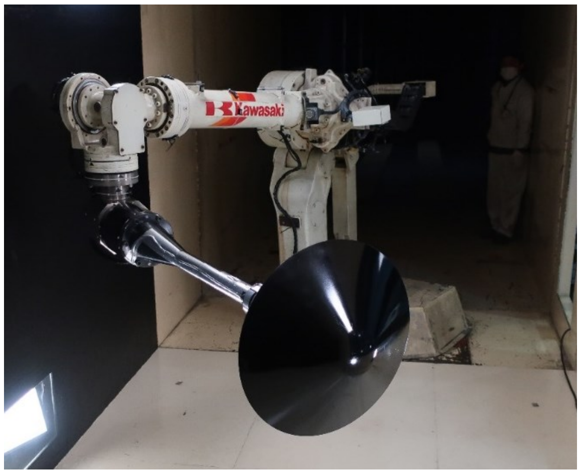

(a) Photograph

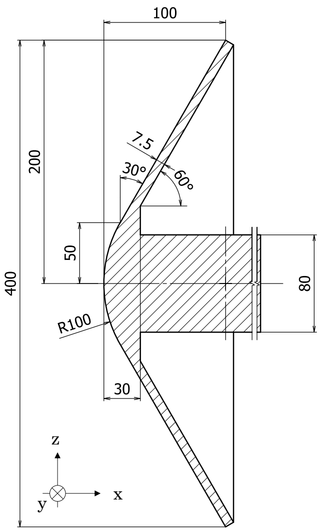

(b) Shape

Fig. 7 Thin aeroshell capsule in the low-speed wind tunnel test

The experimental conditions are listed in Table 4. The AOA was set by horizontally swinging the sting.

Table 4 Experimental conditions

for low-speed wind tunnel tests

Diameter of model, m	0.4
Angle of attack, deg	-50–50
Velocity, m/s	10–50

3.2 Transonic and supersonic wind tunnel test

The TWT and SWT were blow-down facilities. Both test section sizes had a 0.6 × 0.6 m square cross-section. The measurement equipment used is presented in Table 5.

Table 5 Measurement equipment used in the TWT and SWT test

Six-components balance	LMC-6522-25
Pressure gauge for atmospheric pressure	MT110, Yokogawa
Pressure gauge for total pressure	CPT6100, Mensor
Pressure gauge for static pressure	CPT6180, Kyowa
Data logger	EDX-3000

Figure 8 shows the shape of the capsule used in the TWT and SWT experiments. The aerodynamic characteristics were measured using a six-component balance attached to the sting, where the capsule was fixed. The time-averaged aerodynamic coefficients were obtained by measuring for approximately 2 s at a sampling rate of 100 Hz. The experimental conditions are listed in Table 6. The AOA was set by vertically swinging a sting.

Table 6 Experimental conditions for TWT and SWT tests

Diameter of model, m	0.08
Angle of attack, deg	-6 ~ 15
Mach number	0.3 ~ 1.3 (TWT)
	1.7 ~ 4.0 (SWT)
Reynolds number	0.77 x10^6 ~ 1.90 x10^6 (TWT)
	2.23 x10^6 ~ 1.49 x10^6 (SWT)

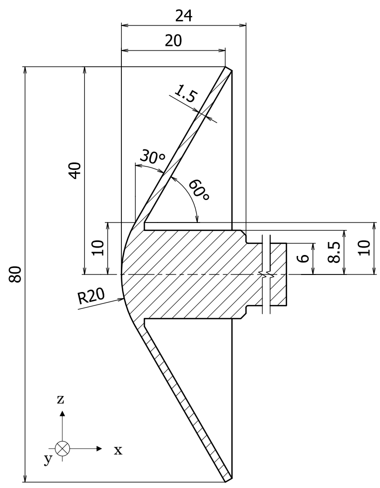

Fig. 8 Thin aeroshell capsule used in the TWT and SWT

4. Numerical method

4.1. Flow field modeling

We assumed that the flow in the low-speed wind tunnel is unsteady and continuum. The gas considered was air, which was composed of 0.765 N_2 and 0.235 O_2 in the mass fraction and was an ideal gas.

The governing equations of the flow field were the compressible Navier–Stokes equations, which are composed of the total mass, momentum, total energy, and equation of state. The molecular viscosity was evaluated using Sutherland's law. Thermal conductivity was calculated using the viscosity, specific heat at constant pressure, and Prandtl number, which was set to 0.72.

The large-eddy simulation (LES) approach was adopted to reproduce the unsteady turbulent flow around the capsule and was filtered using Favre filtering. The standard Smagorinsky model [21] is used as the subgrid-scale (SGS) model. The SGS eddy viscosity μ_{SGS} was obtained as follows:

$$\mu_{\mathrm{SGS}} = \rho L_{\mathrm{SGS}} \sqrt{2\bar{S}_{ij}\bar{S}_{ij}}, \quad (4)$$

where $\bar{S}_{ij}$ represents the strain rate tensor. The mixing length L_{SGS} and grid scale Δ can be expressed [22] as

$$L_{\mathrm{SGS}} = \min(kd, C_{\mathrm{s}}\Delta), \quad (5)$$

$$\Delta = \min[\max(C_{\mathrm{w}}d, C_{\mathrm{w}}\Delta_{\max}, \Delta_{wn}), \Delta_{\max}], \quad (6)$$

where $k, C_{\mathrm{s}}, d, C_{\mathrm{w}}, \Delta_{\max},$ and $\Delta_{\min}$ represent the von Karman constant ($k = 0.41$), Smagorinsky constant ($C_{\mathrm{s}} = 0.2$), distance from the surface, empirical constant ($C_{\mathrm{w}} = 0.15$), maximum grid size in each direction, and minimum value, respectively. The SGS thermal conductivity was calculated using the SGS eddy viscosity, specific heat at constant pressure, and turbulent Prandtl number of 0.90.

The governing equations were solved using a node-centered finite-volume approach. The evaluation of the advection fluxes across the cell interface in the equations was performed using the simple low-dissipation advection upstream splitting method scheme (SLAU) [23], with the monotonic upstream-centered scheme for conservation laws (MUSCL) interpolation method for high accuracy. Furthermore, the viscous fluxes were calculated using the average value between the gradients of the neighboring computational cells. The Green–Gauss method was adopted to calculate the spatial gradients of flow properties. Moreover, time integration was performed using an implicit time marching approach. A dual-time-stepping method with a second-order backward difference was adopted for the time integration in the unsteady state. Inner iterations were performed using the local time-stepping method, and outer iterations were performed using the global time-stepping method for efficient time integration. The matrix solver of the governing equation system was the flexible generalized minimal residual method (FGMRES) [24] with the lower-upper symmetric Gauss–Seidel method (LU–SGS) [25].

The numerical models were implemented using the open-source solver SU2-v7.0.3 [26]. The SGS model of the LES was added to the software by the authors. Parallel computations were performed on the "Grand Chariot" computer system of the Hokkaido University Information Initiative Center using the domain decomposition method and message passing interface (MPI).

4.2. Computational conditions

Figures 9 and 10 show the computational domains for reproducing the flow fields in LWT, TWT, and SWT. The sting and walls of the wind tunnel were not considered in the computations. The grids in the computational domain were composed of hexahedral meshes. The total number of computational cells was approximately 10.4 million, and the minimum cell width was 3.0e-6 m for LWT and TWT. That was approximately 11.3 million, and the minimum cell width was 3.0e-7 m for SWT. Figure 11 shows the shape of the capsule used in the analysis.

At the inlet, the freestream variables are given by the conditions in Table 7. A far-field boundary condition was imposed at the outlet. Furthermore, a nonslip condition for the velocity and no pressure gradient condition normal to the surface were imposed at the boundary on the surface of the capsule. The surface temperature was fixed at 300 K, which is close to the experimental conditions.

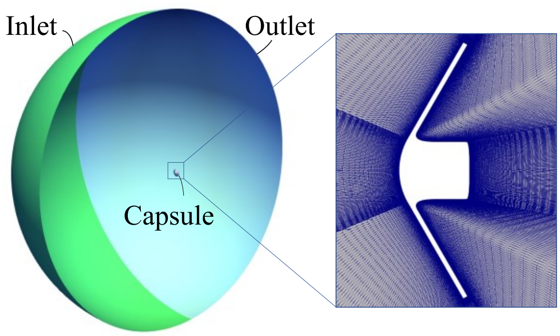

Fig. 9 Computational domain for LWT and TWT

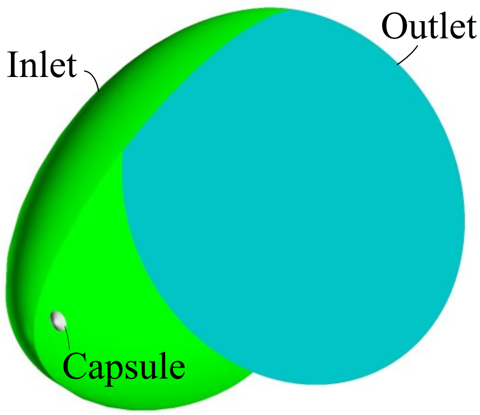

Fig. 10 Computational domain for SWT

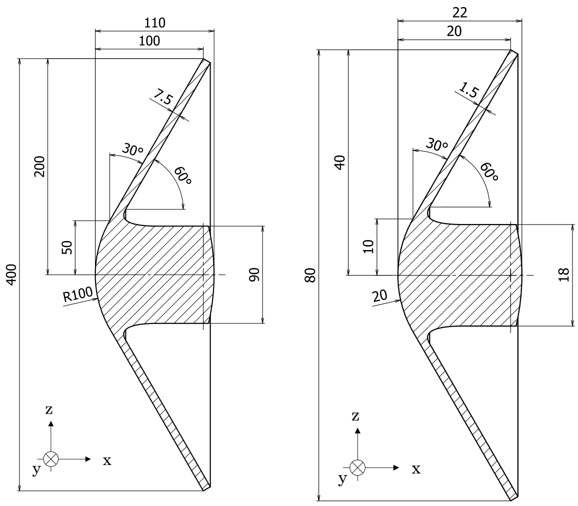

(a) for LWT (b) for TWT and SWT

Fig. 11 Shapes of the capsule in the analysis

Table 7 Freestream conditions for numerical simulations

	LWT	TWT	SWT
Velocity, m/s	50.0	340.0	676.1
Density, kg/m^3	1.15	1.05	0.16
Pressure, Pa	1.02 x10^5	7.18 x10^4	3.20 x10^3
Temperature, K	301.5	238.0	69.9
Reynolds number	1.24 x10^6	1.86 x10^6	1.83 x10^6
Mach number	0.146	1.1	4.0

5. Results and discussion

5.1. Flow fields

The PIV results were compared with the numerical results to evaluate the flow field structure around the capsule. Figure 12 shows the mean velocity distributions for AOAs of 0 °, 15 °, and -15 ° AOA in the experiment and analysis of the LWT. In Fig. 12, six images are overlaid to depict a larger flow field. The magnitudes of the vectors in these figures are constant. The PIV result at 0 ° in the AOA indicates that a recirculation region was formed in the wake. The same vortices were confirmed in the CFD results at 0 ° in the AOA. This indicates that the numerical results qualitatively agree with the experimental results. Additionally, based on an unsteady analysis conducted using CFD, it was confirmed that detachment from the shoulder region and vortex shedding occurred. Furthermore, a recirculation region was formed as the time average of these flows. The primary vortex for ±15 ° in the AOA was qualitatively in good agreement with the experimental and numerical results.

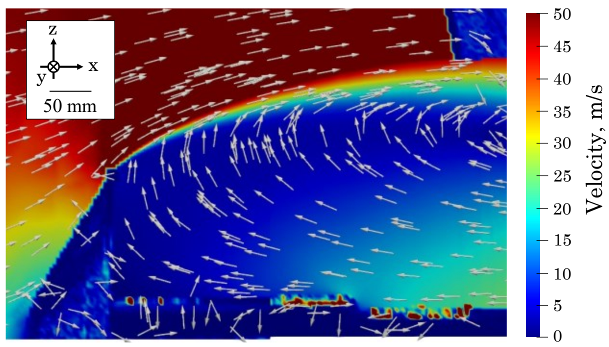

(a) 0 ° AOA (PIV)

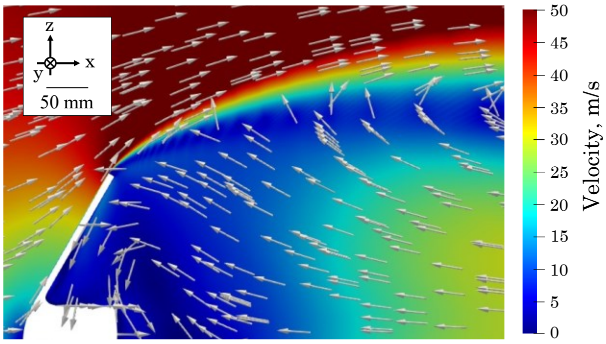

(b) 0 ° AOA (CFD)

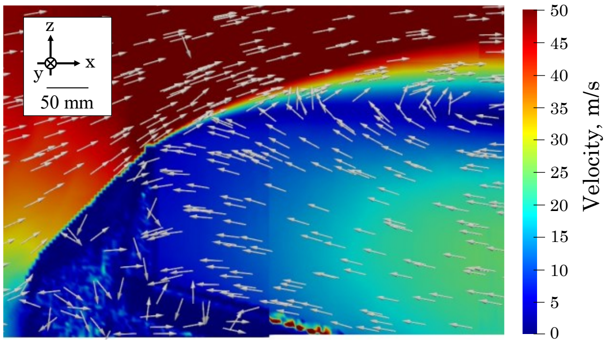

(c) 15 ° AOA (PIV)

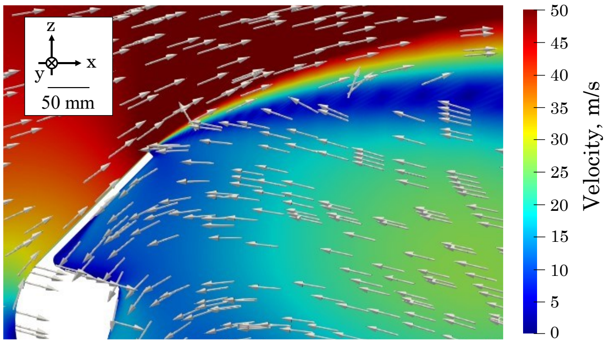

(d) 15 ° AOA (CFD)

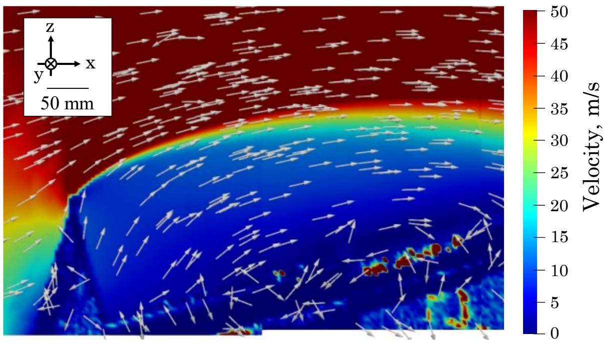

(e) -15 ° AOA (PIV)

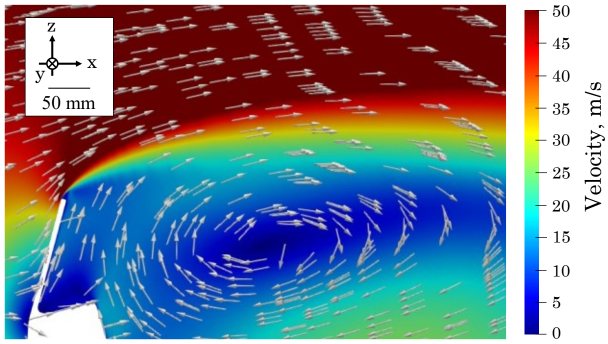

(f) -15 ° AOA (CFD)

Fig. 12 Mean velocity distributions with normalized vector field in the LWT

Figures 13 and 14 show the mean Mach number distributions in the TWT and SWT, respectively. The flow fields were qualitatively similar, confirming a shock wave in front of the capsule. In addition, a recirculation area was formed at the rear of the capsule, and the flow separated from the shoulder accelerated, indicating that the flow was expanding. Furthermore, the expanded flow resulted in the formation of a recompressed region. Moreover, downstream of the recirculation region behind the capsule, steady vortex shedding was observed.

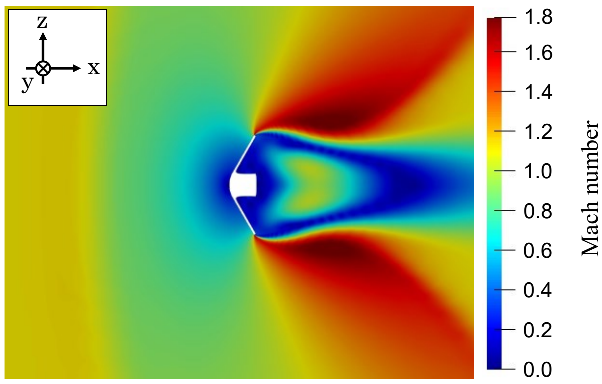

Fig. 13 Mean Mach number distributions at 0 degrees AOA for Ma1.1 in the TWT

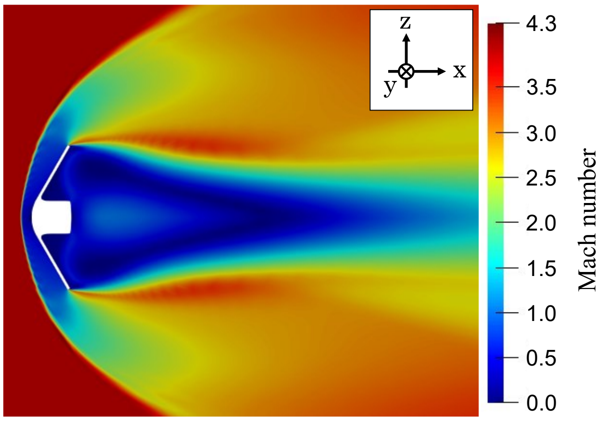

Fig. 14 Mean Mach number distributions at 0 ° AOA for Ma4.0 in the SWT

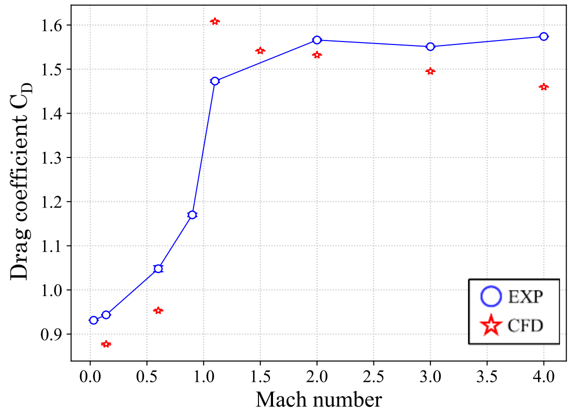

Fig. 15 Drag coefficient in the all-speed range

5.2. Aerodynamic coefficients

The profiles of the drag against the Mach number are shown in Fig. 15. The drag coefficient increased with increasing Mach numbers up to Mach 1, owing to the increase in wave drag caused by the compression of the gas in front of the capsule. In regions greater than Mach 1, the position of separation was clear, and no shock wave was attached to the capsule. Therefore, the drag coefficient did not fluctuate significantly. The drag coefficients between the experiment and analysis agreed well and the errors were within 10 %. Based on previous research [27] and considering CFD alone, a higher C_D value is expected in the absence of a sting. However, in experimental scenarios where the diameter was close to 80 mm, a smaller C_D value was observed compared with smaller diameters. These combined effects suggest that the experimental C_D value in TWT decreased. Additionally, the blockage ratio influences the force in the x-direction, causing a larger C_D.

The profiles of the drag and lift coefficients against AOA are shown in Figs. 16 and 17, respectively. The drag coefficient in the experiment did not have a maximum value at 0° in the LWT experiment, whereas the profile of the drag coefficients was expected to be convex upward with the vertex at 0°. Furthermore, this was a convex upward distribution in the numerical analysis without a sting. Therefore, the large sting behind the capsule affects the drag. Comparing the experimental and numerical results, an error of more than 15 % in the drag coefficient is observed for LWT. Based on the results of the analysis at 0° AOA, the ratio of the drag at the front to that at the rear was 0.515. Sting was one of the factors that increased the error. In addition, the blockage ratio of the wind tunnel test section was also a factor in the error. The ratio of the cross-sectional area of the flow to the projected area of the model was defined as follows:

$$\text{Blockage ratio} = \frac{\text{projected area of model}}{\text{area of cross-section}} \times 100. \quad (7)$$

This value was used to evaluate the influence of the wind tunnel wall. In this experiment, it was approximately 3.1 % for the LWT case, which could be also one of the error factors. It was indicated that the drag coefficient increased owing to the stagnation of the flow in front of the model. The errors in drag coefficient between the experiment and analysis were within 10 % for the cases of TWT and SWT. This was because the blockage ratio was 1.4 % and the velocity of flow was high, which reduced the effect of the wall. Additionally, the effect of the blockage rate, which has a large effect in the axial direction, is small at a low AOA because the lift coefficient depends on the force in the radial direction. Thus, the lift coefficients between the experiment and analysis agreed well for all the cases.

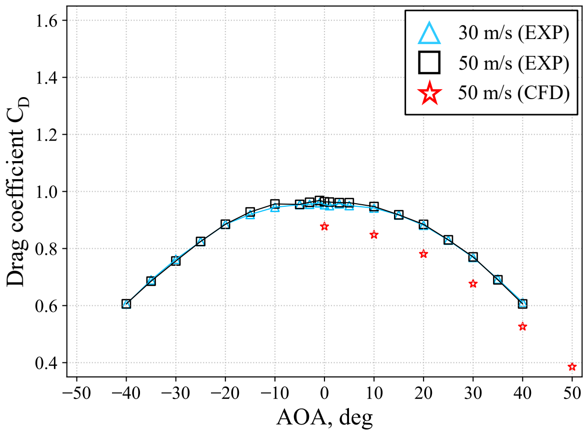

(a) LWT

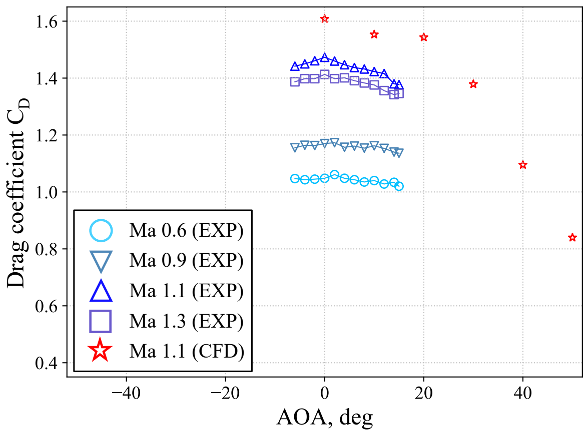

(b) TWT

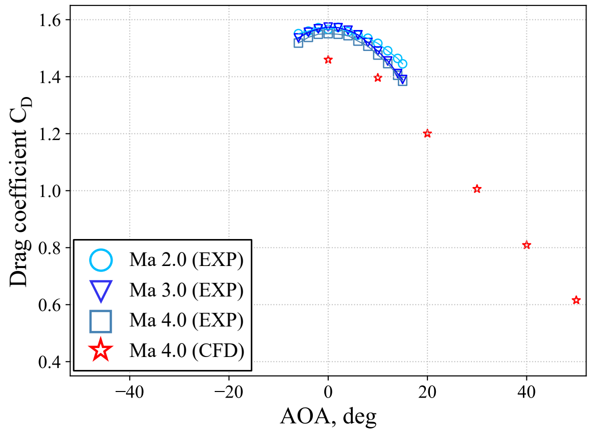

(c) SWT

Fig. 16 Comparison of drag coefficient against AOA between wind tunnel experiment and CFD

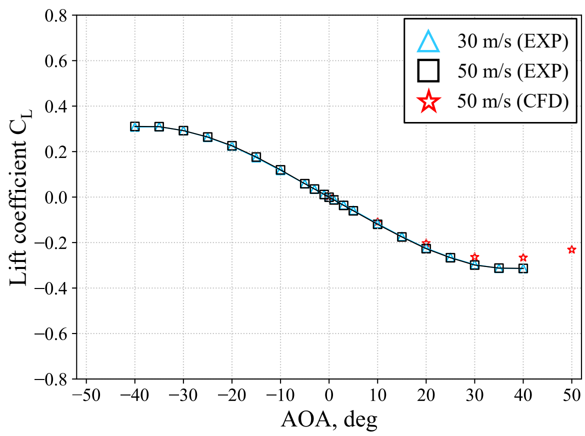

(a) LWT

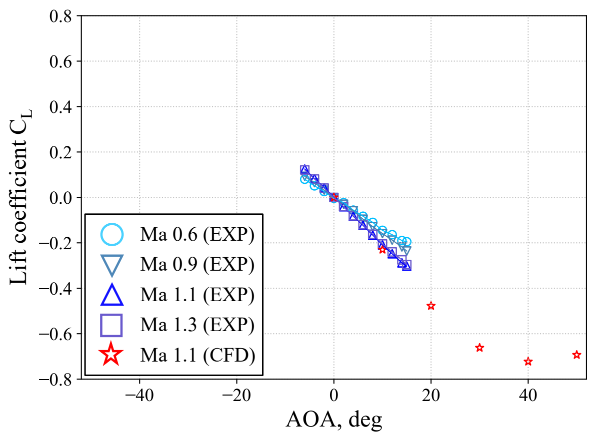

(b) TWT

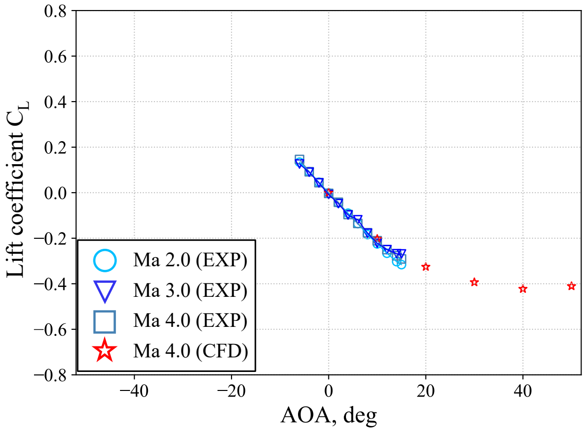

(c) SWT

Fig. 17 Comparison of left coefficient against AOA between wind tunnel experiment and CFD

5.3. Static stability

Figure 18 shows the plots of the pitching moment coefficient against the AOA for each wind tunnel. The experimental results confirmed that there is a negative moment from the positive AOA and a positive moment from the negative AOA when the center of gravity is located at the front and rear ends of the capsule. This indicated that the capsule was statically stable in all speed regions when the center of gravity was located inside the model on the centerline. The CFD results qualitatively indicated the same pattern as the experiments, whereas some deviations between the experimental and numerical results appeared.

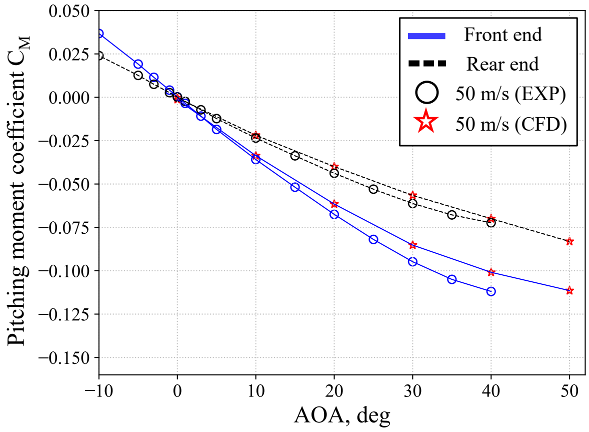

(a) LWT

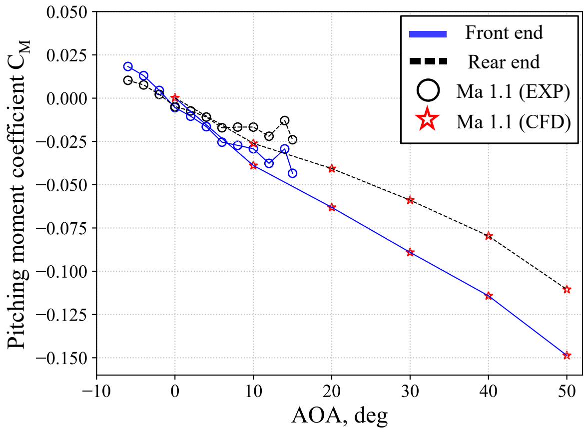

(b) TWT

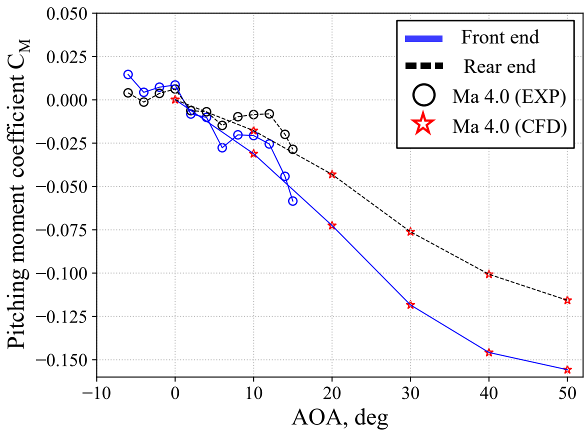

(c) SWT

Fig. 18 Comparison of Pitching moment coefficient against AOA between wind tunnel experiment and CFD

5.4. Mechanism of static stability

Figure 19 shows the distribution of the mean pressure coefficient on the surface obtained from the analysis. At 0° AOA, the pressure distribution was symmetrical around the body axis. The pressure on the front surface was sensitive to the change in AOA, whereas the pressure on the rear surface was not. Table 8 lists the contributions to the moments on the front and rear sides. In almost all cases where the angle was greater than 10°, the contribution of the rear was less than 10 %, indicating that the moment of the front side has a significant influence. Therefore, as shown in Fig. 20, the pressure on the windward side of the front surface increased and the pressure on the leeward side of the front surface decreased when the AOA was increased. In Table 8, the pressure on the windward side generated a moment in the direction that canceled the change in the AOA because the pressure on the rear surface was almost constant compared with that on the front surface. This was considered statistically stable.

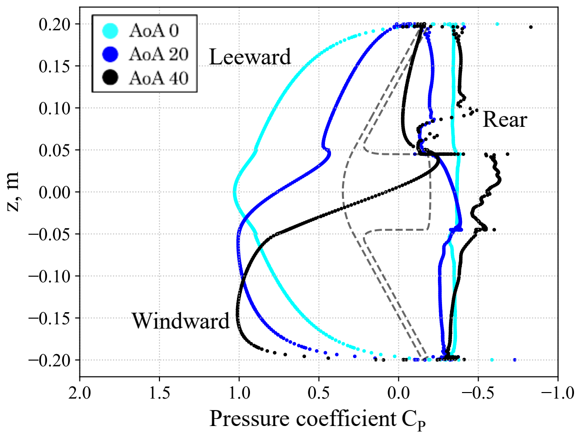

(a) LWT (Ma 0.14)

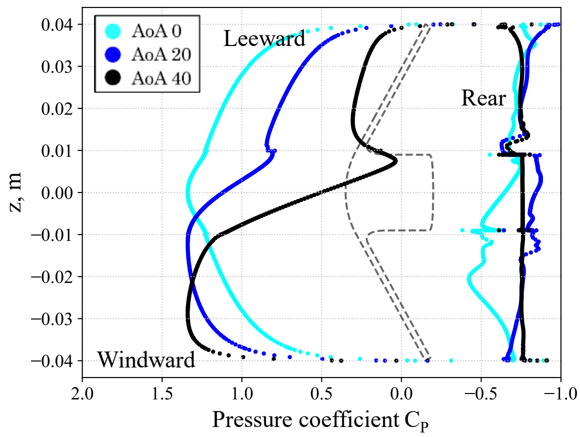

(b) TWT (Ma 1.1)

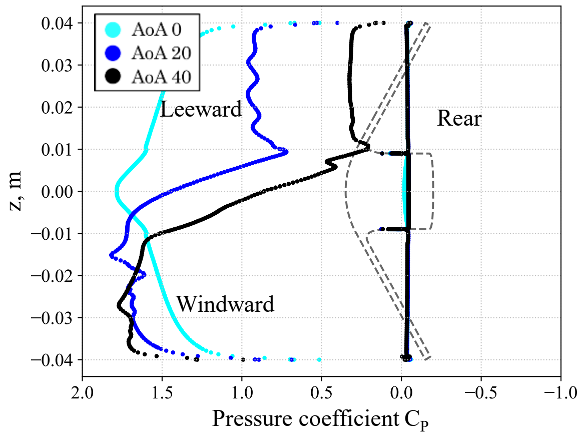

(c) SWT (Ma 4.0)

Fig. 19 Distribution of mean pressure coefficient on the surface of the capsule at each AOA from CFD results

Table 8 Contributions to the moment at the front and back side from CFD results

AOA, degree	Ratio of the moment at the rear to that at the front, %		
	LWT (Ma 0.14)	TWT (Ma 1.1)	SWT (Ma 4.0)
0	-	-	-
10	8.1	32	0.88
20	1.4	7.6	0.31
30	-3.6	2.8	0.22

40	-8.5	0.26	0.30
50	-6.6	0.40	0.26

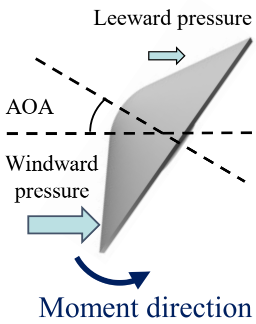

Fig. 20 Image of static stability mechanism

6. Conclusion

In this study, we propose a novel sample-return capsule for deep-space exploration. The aerodynamic stability of the attitude is one of the most important issues for a capsule. Therefore, an experiment was conducted using a 2 × 2 m low-speed, transonic, and supersonic wind tunnel at JAXA to evaluate the static stability of the thin aeroshell-type reentry capsule at low speed. Additionally, numerical analysis was conducted to investigate the static stability mechanism.

This capsule decelerated at a higher altitude owing to a lower ballistic coefficient, according to the trajectory analysis results. The peak heat flux at the stagnation point was suppressed compared with that of the Hayabusa capsule.

In the experimental results, the thin aeroshell capsule was statically stable at all speeds, regardless of where the center of gravity was located on the centerline inside it. Furthermore, a recirculation region had formed behind the capsule.

The mechanism of static stability in the attitude based on the results of the numerical analysis is described as follows: When the angle of attack was applied, there was a difference in pressure between the leeward and windward sides of the front surface. This difference in the pressure distribution caused the moment in the direction that canceled the angle of attack.

In this study, we investigated static stability at all speeds. However, the dynamic stability of the flow during reentry was not investigated. To confirm whether the capsule is dynamically stable over the entire speed range, wind tunnel tests, balloon drop tests, and numerical analyses must be conducted in future studies.

Acknowledgments

This study was supported by JSPS KAKENHI (Grant No.20H02360) and JST SPRING (Grant Number JPMJSP2119). We used the computational resources of the Grand Chariot computer provided by Hokkaido University and the supercomputer Fugaku provided by the RIKEN Center for Computational Science (Project ID: hp210266). The wind tunnel experiments were conducted at a low-speed wind tunnel facility, transonic wind tunnel, and supersonic wind tunnel provided by the Japan Aerospace Exploration Agency as an inter-university research institute facility (Project ID: LWT2-20-01, W20-001). We also appreciate the LWT2 team and the optical measurement team of JAXA for their technical supports on the series of wind tunnel experiments (LWT2-21-19/OPT-21-11-06).

References

[1] Kazuhiko, Y., Toshiyuki, S., Hiroki, T., Takashi, O., Aoi, H., Tomonari, H.: Proposal for Advanced Sample Return Capsule for Deep Space Exploration with Small Spacecraft. Proceedings of 64th Space Sciences and Technology Conference in Japan, JSASS-2020-4626-4F02 (2020)

[2] Wu, R., Roberts, ,P.C.E., Xu, L., Soutis, C., Diver, C.,: Deployable self-regulating centrifugally-stiffened decelerator (DESCENT): Design scalability and low altitude drop test, Aerospace Science and Technology. **114**, 106710 (2021). https://doi.org/10.1016/j.ast.2021.106710

[3] Takahashi, Y., Koike, T., Oshima, N., Yamada, K.: Aerothermodynamic analysis for deformed membrane of inflatable aeroshell in orbital reentry mission. Aerospace Science and Technology. **92**, 858–868 (2019). https://doi.org/10.1016/j.ast.2019.06.047

[4] Nagata, Y., Yamada, K., Abe, T., Suzuki, K.: Attitude Dynamics for Flare-type Membrane Aeroshell Capsule in Reentry Flight Experiment. in: AIAA Aerodynamic Decelerator Systems (ADS) Conference, American Institute of Aeronautics and Astronautics (2013). https://doi.org/10.2514/6.2013-1285

[5] Hiraki, K.: Experimental Study on Dynamic Instability of Capsule-shaped Body. ISAS Rep. **103**, 1–55 (1999)

[6] Wright, B.R., Kilgore, R.A.: Aerodynamic Damping and Oscillatory Stability in Pitch and Yaw of Gemini Configurations At Mach Numbers From 0.50 To 4.63. NASA-TN-D-3159 (1996). https://ntrs.nasa.gov/search.jsp?R=19660005466

[7] Kazemba, C.D., Braun, R.D., Clark, I.G., Schoenenberger, M.: Survey of blunt-body supersonic dynamic stability. Journal of Spacecraft and Rockets. **54**, 109–127 (2017). https://doi.org/10.2514/1.A33552

[8] Beam, B.B.H., Hedstrom, C.E.: Damping in Pitch of Bluff Bodies of Revolution at Mach Numbers from 2.5 to 3.5. NASA TM X-90 (1959)

[9] Uselton, B.L., Wallace, A.R.: DAMPING-IN-PITCH AND DRAG CHARACTERISTICS OF THE VIKING CONFIGURATION AT MACH NUMBERS FROM 1.6 THROUGH 3. Arnold Engineering Development Complex TR 70-49 (1972)

[10] Sammomds, R.: Transonic static- and dynamic-stability characteristics of two large-angle spherically blunted high-drag cones. in: Propulsion and ASW Meeting, American Institute of Aeronautics and Astronautics (1970). https://doi.org/10.2514/6.1970-564

[11] Chapman, G.T., Berner, C., Hathaway, W., Winchenbach, G.L., Mitcheltree, R.: The use of spherical bases to eliminate limit cycles of blunt entry vehicles. 37th Aerospace Sciences Meeting and Exhibit (1999). https://doi.org/10.2514/6.1999-1023

[12] Teramoto, S., Hiraki, K., Fujii, K.: Numerical analysis of dynamic stability of a reentry capsule at transonic speeds. AIAA Journal. **39**, 646–653 (2001). https://doi.org/10.2514/2.1357

[13] Baillion, M.: BLUNT BODIES DYNAMIC DERIVATIVES. Capsule Aerothermodynamics, NATO Advisory Group for Aerospace Research and Development Rept. AGARD-R-808 (1997)

[14] Takasawa, H., Fujii, T., Hirata, K., Moriyoshi, T., Takahashi, Y., Nagata, Y., Yamada, K.: Dynamic Instability of a Thin-Shell Type Aeroshell Capsule with Pitching Motion in Transonic wind Tunnel. Aerospace Europe Conference Joint 10th EUCASS – 9th CEAS Conference. AEROFLIPHY 4 , (2023).
Website: https://eucass-ceas-2023.eu/

[15] Yamada, T., Ishii, N., Inatani, Y., Yamada, K., Hiraki, K.: Technology and Re-entry Flight of Hayabusa Capsule. Aeronautical and Space Sciences in Japan. **60**, 192–197 (2012). https://doi.org/10.14822/kjsass.60.5_192

[16] Takahashi, Y., Saito, M., Oshima, N., Yamada, K.: Trajectory reconstruction for nanosatellite in very low Earth orbit using machine learning. Acta Astronautica. **194**, 301–308 (2022). https://doi.org/10.1016/j.actaastro.2022.02.010

[17] Picone, J. M., Hedin, A. E., Drob, D. P., and Aikin, A. C.: NRLMSISE-00 empirical model of the

atmosphere: Statistical comparisons and scientific issues. J. Geophys. Res. **107**(A12), 1468 (2002). https://doi.org/10.1029/2002JA009430

[18] Kemp, N.H., Riddell, F.R.: Heat Transfer to Satellite Vehicles Re-entering the Atmosphere. Journal of Jet Propulsion. **27**, 132–137 (1957). https://doi.org/10.2514/8.12603

[19] Tauber, M.E., Sutton, K.: Stagnation-point radiative heating relations for earth and Mars entries. Journal of Spacecraft and Rockets. **28**, 40–42 (1991). https://doi.org/10.2514/3.26206

[20] Kato, H., Koike, S., Nakakita, K.: Time-Resolved Stereoscopic PIV Measurement of Unsteady Wingtip Flowfield. 50th AIAA Aerospace Sciences Meeting including the New Horizons Forum and Aerospace Exposition (2012). https://arc.aiaa.org/doi/abs/10.2514/6.2012-35

[21] Smagorinsky, J.: GENERAL CIRCULATION EXPERIMENTS WITH THE PRIMITIVE EQUATIONS. Monthly Weather Review. **91**, 99–164 (1963). https://doi.org/10.1175/1520-0493(1963)091<0099:GCEWTP>2.3.CO;2

[22] Shur, M.L., Spalart, P.R., Strelets, M.K., Travin, A.K.: A hybrid RANS-LES approach with delayed-DES and wall-modelled LES capabilities. International Journal of Heat and Fluid Flow. **29**, 1638–1649 (2008). https://doi.org/10.1016/j.ijheatfluidflow.2008.07.001

[23] Shima, E., Kitamura, K.: Parameter-Free simple Low-Dissipation AUSM-Family scheme for all speeds. AIAA Journal. **49**, 1693–1709 (2011). https://doi.org/10.2514/1.J050905

[24] Saad, Y.: A Flexible Inner-Outer Preconditioned GMRES Algorithm. SIAM Journal on Scientific Computing. **14**, 461–469 (1993). https://doi.org/10.1137/0914028

[25] Jameson, A., Yoon, S.: Lower-upper implicit schemes with multiple grids for the Euler equations. AIAA Journal. **25**, 929–935 (1987). https://doi.org/10.2514/3.9724

[26] Economon, T.D., Palacios, F., Copeland, S.R., Lukaczyk, T.W., Alonso, J.J.: SU2: An open-source suite for multiphysics simulation and design. AIAA Journal. **54**, 828–846 (2016). https://doi.org/10.2514/1.J053813

[27] Yusuke, T., Manabu, M., Nobuyuki O., Kazuhiko, Y.: Drag Behavior of Inflatable Reentry Vehicle in Transonic Regime. Journal of Spacecraft and Rockets. **56**, 2, 577–585, (2019). https://doi.org/10.2514/1.A34069